Two-Dimensional Modeling of Nonlinear Dynamics of Forcespinning Jet Formation

Dumitru I. Caruntu[1]
Fellow ASME
Mechanical Engineering Department,
University of Texas Rio Grande Valley,
Edinburg, TX 78539
e-mails: dumitru.caruntu@utrgv.edu;
caruntud2@asme.org, dcaruntu@yahoo.com

Simon Padron
Mechanical Engineering Department,
University of Texas Rio Grande Valley,
Edinburg, TX 78539

Karen Lozano
Mechanical Engineering Department,
University of Texas Rio Grande Valley,
Edinburg, TX 78539

Forcespinning is a novel method that makes use of centrifugal forces to produce nanofibers rapidly and at high yields. To improve and enhance the forcespinning production method, a 2D computational forcespinning inviscid fluid dynamics model is developed. Two models, namely, time-independent and time-dependent, are obtained in order to investigate the effects of various parameters on fiber forcespinning formation (trajectory, jet diameter, tangential velocity). The fluid dynamics equations are solved using the method of multiple scales along with the finite difference method and including slender-jet theory assumptions. It is important to produce jets with small diameters in the micro- and nanorange. Both the Weber (We) and Rossby (Rb) numbers were found to expand the jet trajectory as they increased. Increasing We and/or decreasing Rb was found to decrease the jet diameter. Also, by varying forcespinning parameters, it has been found that the jet radius can be decreased by increasing the jet exit angle in the direction of rotation, reducing the spinneret fluid level, increasing the angular velocity of the spinneret, reducing spinneret length, and/or reducing the orifice diameter. Knowing that jet trajectories are important for designing and positioning of the fiber collector, it has been found that the trajectories expand out with the increase in the jet exit angle in the direction of rotation, increase in the fluid level, increase in the angular velocity, and/or increase in the spinneret length. Production rates and jet radii for any predetermined radial collector distance were also determined. [DOI: 10.1115/1.4051167]

1 Introduction

Nanofibers have attracted much attention recently due to the improved characteristics of materials when manufactured into such small sizes. One of the most prominent characteristics of nanofibers is the large surface area to volume ratio which dramatically increases the surface functionality. Nanofibers have also shown to exhibit improved mechanical and thermal properties due to the induced alignment during the elongation process. Electrospinning and meltspinning methods are largely used to produce nanofibers. Most nanofiber production to date focuses on the use of electrospinning methods. These methods use high voltages to produce nanofibers, and much experimental work has been done on the subject with many types of polymers [1,2]. In the electrospinning process, the usual setup consists of a syringe with a metallic needle, a high-voltage power supply, a grounded target collector, and a syringe pump. The desired polymer solution is introduced to the syringe and then pushed through the needle at a constant feed rate by the syringe pump, forming a droplet at the end of the needle, called the Taylor cone. The driving force is then created by applying a high voltage (usually between 5 and 30 kV) between the tip of the needle and the grounded target collector. This method is very successful in producing nanofibers. However, its main drawbacks are the low yield that does not allow for time efficient mass production and the difficulty of producing fibers from melts. The modeling of electrospinning deals with electrohydrodynamics. Works on straight liquid jets produced by such forces have been reported in the literature [3–8]. The modeling of such jets has its foundations on the work done by Raleigh [9] and Weber [10], who focused on the formation and instability of liquid jets under gravitational forces. A thorough review on axisymmetric liquid jets is presented by Eggers [11]. Ozgen and Uzol [12] investigated the instability characteristics of a liquid jet discharging from a nozzle. Meltspinning is another method of fiber production. This method has high yield outputs. However, the fiber diameters at their smallest lie within the low micrometer range [13].

A newly developed method of producing nanofibers, called forcespinning (FS), has proven to be an excellent alternative way for producing polymer nanofibers. Unlike electrospinning, which draws fibers through the use of electrostatic force, FS utilizes centrifugal force which allows for a whole new host of materials to be used while providing mass production capabilities. The process works by loading the polymer solution into a special spinneret that rotates the fluid and expels it as jets that result in nanofibers which are collected on a collector at a certain distance away from the center of spinneret rotation. The novel FS method ejects fibers radially outward onto a collector producing nanofibers already confirmed experimentally to be as small as 50 nm in diameter. In order to attain full control on the final nanofiber diameters, a complete understanding must be attained on various system parameters such as intrinsic properties of the system (e.g., viscoelasticity and surface tension) and processing parameters (e.g., angular velocity, exit nozzle, and distance to the collector), which influence the rotational forces ultimately responsible for highly curved trajectories of emerging jets that are subsequently stretched into fine fibers. Various investigations on the study of curved liquid jets, starting with Weber [10], have been conducted. Wallwork et al. [14], Decent et al. [15], and Uddin and Decent [16] analyzed the formation and stability of droplets under rotating forces in a process known as prilling, which is used for the manufacturing of detergents and fertilizers. Dravid et al. [17] investigated drop formation in non-Newtonian jets. One-dimensional model investigating the breakup process in the case of capillary liquid jets has been report by Ahmed et al. [18].

When producing nanofibers by the FS method, it is required that the polymer is in liquid form. This can be obtained either by preparing a polymer solution or by melting. The properties associated with the polymer solution or melt play a significant role in determining the resulting fiber diameter and morphology. As the polymer is drawn, two important polymer properties that need to be considered, namely, surface tension and viscosity. Since the

[1]Corresponding author.

Manuscript received October 22, 2019; final manuscript received May 2, 2021; published online June 17, 2021. Assoc. Editor: Bogdan I. Epureanu.

polymers also possess elastic properties, the stretching rates and relaxation times must also be considered. Another important factor is the rate of solvent evaporation, which has an effect on the polymer's viscosity and elasticity. In order to produce nanofibers, surface tension must be overcome by the centrifugal force.

Barhoum et al. [19] developed a comprehensive review and comparison of the available techniques to produce nanofibers.

Computational methods are often desirable to aid in the optimization of the parameters needed to produce fibers. Various one-dimensional electrospinning models have been proposed with a focus on the effects of the rheological properties of the polymer solutions on fiber formation [20–22]. Models incorporating the effects of solution viscosity, solvent evaporation, solidification, surface tension, and electric forces have been reported. These models describe all the stages of the electrospinning process using both linear and nonlinear models [23,24]. A theoretical model describing the whole electrospinning process is described by Thompson et al. [5]. The viscoelastic model used in this case is the upper-convected Maxwell model, as described in Refs. [7] and [23]. The polymer solutions also depend on the solvent concentration; for this reason, the equations are also supplemented by the equations describing solvent evaporation from the jet [7]. The model predicts the path of the jet driven by the bending instability. The equations are described in more detail by Thompson et al. [5].

In the past 20 years, there have been a number of papers reporting models of the dynamics of liquid jets based on slender jet theory and applied to forcespinning [14,15,25–30] and forcespinning experimental work [31].

Walwork et al. [14] investigated a spiraling slender inviscid liquid jet to include surface tension and with the assumption that the centerline of the jet was stationary. They calculated the linear jetting stability by using asymptotic methods and predicted the breakup length of the jet. It has also been found that the trajectory of the jet became more tightly coiled as We increased. Decent et al. [15] reported a model for the dynamics of an inviscid liquid jet emerging from a rotating drum. Both surface tension and gravity have been included in the model. They used asymptotic methods to find the steady-state solutions, investigated both temporal and spatial stability of the jet, and reported that axisymmetric mode can be unstable. Parau et al. [25] reported the effect of a disturbance on a slender rotating jet using an asymptotic approach. They reported the steady solutions for the liquid jet and the effect of viscosity on the trajectory and the radius of the jet.

Padron et al. [26] reported a two-dimensional slender jet model of the forcespinning process based on the continuity and momentum equations. The rotating jet model included surface tension and boundary conditions of the system and reported numerical simulations predicting the fiber trajectory and fiber radius for various values of We and Rb numbers. Increasing the rotation rate, the jet radius decreased. Trajectories contracted with the increasing surface tension. Padron and Caruntu [28] reported a two-dimensional slender jet model of the forcespinning process based on the continuity and momentum equations to include fluid viscosity. They used the method of multiple scales and finite difference method to solve the differential equations of motion. They reported the effect of viscosity on the forcespinning dynamics. Padron et al. [31] reported the experimental work on forcespinning. They experimentally predicted the effects of various parameters such as spinneret angular velocity, aspect ratio, orifice radius and orientation, and fluid viscosity on fiber trajectories and fiber diameters.

Taghavi and Larson [29] proposed a thin-fiber (string) model for a semi-infinite Newtonian viscous fiber emerging from a rotating nozzle. They found the steady fiber velocity and diameter, and showed that for $\mathrm{Rb} < 0.5$ and $\mathrm{Re} < 1$ regularization of the string model equations is required to provide numerical stability, and that for $\mathrm{Rb} > 0.5$ regularization is not necessary.

Riahi [30] used a viscosity model to investigate the properties or fiber jets during the spinning process. He used multiscale and perturbation techniques to develop the governing equations. The expressions of steady solutions for the jet quantities such as radius, speed, stretching rate, strain rate, and trajectory versus arc length as well as the stability of the nonlinear jet versus different types of perturbations were reported.

Models have also been developed for the meltspinning process. In meltspinning, a polymer is heated and pulled through a spinneret by a take-up wheel. Meltspinning has the main advantage of being able to produce fibers up to 10 times faster than melt blowing and up to 100 times faster than electrospinning [32]. However, this method has the disadvantage of not being able to produce fibers with diameters less than 10 μm [13]. There are different meltspinning parameters that have been analyzed. Isothermal and nonisothermal meltspinning methods have been studied in detail [32,33]. In order to address instability problems, external cooling methods have been used [34]. Recently, the effects of external heating in the meltspinning process have been investigated. To model a polymer melt or solution, the viscoelastic properties have to be taken into account. Unlike Newtonian fluids, viscoelastic fluids have the ability to store and dissipate energy, have stress–strain relationships which can affect the jet flow, and exhibit flow instabilities [35–37]. A model presented by Chunfeng et al. [38] describes the process for nonisothermal meltspinning of viscoelastic liquids exhibiting a step-like viscosity variation with temperature. To solve the equations, the authors used a slender-jet approximation.

In this work, a novel 2D inviscid fluid dynamics model for the new FS fiber producing method is developed, and predictions of the effects of parameters on the nanofiber formation are reported. This model is based on the slender inviscid liquid jet theory to include surface tension and neglect gravitational forces and azimuthal motion of the jet, Wallwork et al. [14], and Padron et al. [26]. (1) The model allows for the variation of the jet exit angle and (2) includes the fluid level within the container. The method of multiple scales is used to predict steady-state solutions using the so-called time-independent model. Steady-state jet trajectories and diameters as functions of the arc length are predicted, and they are in good agreement with data reported in the literature [14,26]. (3) This work predicts the effect of Rossby (Rb) and Weber (We) numbers on tangential velocity. The tangential velocity of the jet provides a way for determining production rates. (4) This work predicts the effect of jet exit angle on the jet trajectory, radius, and tangential velocity. The reason for modeling various exit angles is to determine the optimum angle for producing the smallest jet diameters. (4) A time-dependent model is developed using the method of multiple scales, and numerical simulations are conducted. The predictions of the time-dependent model show how steady-state jet trajectory, radius, and tangential velocity are reached in time. (5) The present model predicts the effects of the fluid level, angular velocity of the spinneret, orifice radius, and spinneret radius on the jet trajectory, radius, and tangential velocity. (6) Numerical simulations for different tolerances and jet lengths show that a smaller tolerance for numerical simulations produces better results.

2 Forcespinning Governing Equations

The modeling of the FS fiber formation involves the determination of the trajectory and final diameter size of the fiber due to parameters such as angular velocity of the spinneret, viscoelastic properties of the polymer, collector diameter, radius of the orifice, container radius, orifice exit angle, and solvent evaporation rate. In certain cases, when inertial forces are low, the effects of gravity may also have an effect on the formation of the fibers. The fiber production process begins by first reaching a critical angular velocity that produces a jet. The jet is then reduced in diameter as it expands outward as a spiral and is then collected. A schematic of this process is shown in Fig. 1. Two coordinate systems are used, one fixed *xyz*, and another one rotating *XYZ* which is

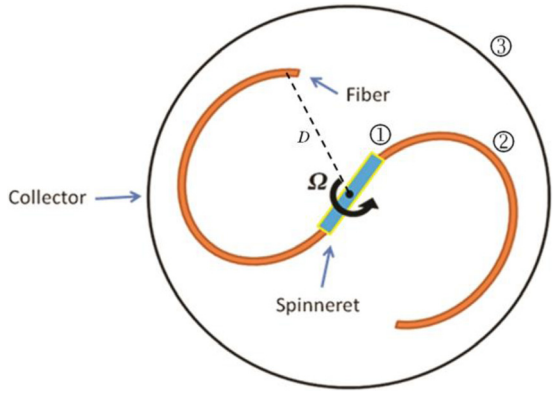

Fig. 1 Forcespinning fiber production process: jet exit, jet diameter reduction, and jet collection [26]

attached to the spinneret, Fig. 2. The governing equations of the system are the continuity equation

$$\nabla \bullet \mathbf{u} = 0 \tag{1}$$

and the momentum equations [26,31,39]

$$\frac{\partial \mathbf{u}}{\partial t} + (\mathbf{u} \cdot \nabla)\mathbf{u} = -\frac{\nabla P}{\rho} + \frac{\nabla \mathbf{T}}{\rho} + \mathbf{g} - \boldsymbol{\omega} \times (\boldsymbol{\omega} \times \mathbf{r}) - 2\boldsymbol{\omega} \times \mathbf{u} \tag{2}$$

where ∇ is the gradient operator, $\mathbf{u} = (u, v, w)$ is the relative velocity of the fiber jet, P is the pressure, $\mathbf{g}$ is the gravity vector, $\mathbf{T}$ is the extra stress tensor, $\boldsymbol{\omega}$ is the angular velocity vector of the spinneret, ρ is the density of the solution, and $\mathbf{r}$ is the position vector of the current centerline point along the fiber. Depending on what constitutive equations are used, the extra stress tensor can be differently represented depending on whether the material is described as inviscid, Newtonian, or viscoelastic [40]. The momentum Eqs. (2) include components due to the local acceleration and convective acceleration on the left-hand side of the equation, and the acceleration due the pressure, extra stress tensor, gravity, along with the Coriolis acceleration, and centrifugal acceleration on the right-hand side of the equation, respectively. The viscoelastic component lies within the stress tensor which depends on the polymer properties most basically described by the strain-rate tensor, polymer viscosity, and polymer relaxation time. Since the fibers experience rapid deformation, nonlinear models such as the upper-convected Maxwell, Phan-Thien Tanner, and Geisiekus models can be used to approximate the polymer material properties [40]. The dimensionless form of the equations provides some important dimensionless numbers that give the ratios between the various forces in the system. Some of these important dimensionless numbers include the Reynolds number, Froude number, Weber number, Rossby number, and Deborah number, which give the ratio of inertial forces to viscous forces, the fiber's inertial force to gravitational force, the fiber's inertial force to surface tension, the fiber's inertial force to Coriolis force, and polymer relaxation to flow time, respectively. The surface tension of a fluid acts at the free surface and is introduced to the model through the fiber boundary conditions. The dynamics of the jet are also described by the arc length condition, $(ds)^2 = (dX)^2 + (dY)^2 + (dZ)^2$, see Eq. (3), the free surface kinematic condition, Eq. (4), dynamic condition Eqs. (5), and (6) and (7) if viscous [41]

$$X_s^2 + Y_s^2 + Z_s^2 = 1 \tag{3}$$

$$\frac{\partial \beta}{\partial t} + \mathbf{u} \bullet \nabla \beta = 0 \quad \text{where} \quad \beta(r,t) = n - R(s, \varnothing, t) = 0 \tag{4}$$

$$\mathbf{n} \cdot \mathbf{T} \cdot \mathbf{n} = \sigma k \quad \text{for} \quad n = R(s, \varnothing, t) \tag{5}$$

$$\mathbf{t}_1 \cdot \mathbf{T} \cdot \mathbf{n} = 0 \quad \text{for} \quad n = R(s, \varnothing, t) \tag{6}$$

$$\mathbf{t}_2 \cdot \mathbf{T} \cdot \mathbf{n} = 0 \quad \text{for} \quad n = R(s, \varnothing, t) \tag{7}$$

where X, Y, and Z are the coordinates of current centerline point O'', Fig. 3, with respect to the rotating Cartesian coordinate system XYZ, Fig. 2, and X_s, Y_s, and Z_s denote partial derivatives of X, Y, Z with respect to the arc length s. $R(s, \varnothing, t)$ defines the fiber's surface and it is the radius of the jet which is to be determined through numerical simulations, σ is the surface tension, and n is the radial distance from the centerline. The curvature k of the surface is given by

$$k = \nabla \mathbf{n} \tag{8}$$

where $\mathbf{n}$ is the unit vector normal to the surface

$$\mathbf{n} = \frac{\nabla \beta}{|\nabla \beta|} \tag{9}$$

and $\mathbf{t}_1$ and $\mathbf{t}_2$ are the tangent unit vectors [25] as follows:

$$\mathbf{t}_1 = \frac{1}{h_s}\frac{\partial \mathbf{r}_\mathbf{A}}{\partial s}, \quad \mathbf{t}_2 = \frac{1}{h_\varnothing}\frac{\partial \mathbf{r}_\mathbf{A}}{\partial \varphi} \tag{10}$$

where $\mathbf{r}_\mathbf{A}$ describes a point on the jet and h_s and $h_\varnothing$ are scale factors. In the kinematic condition, Eq. (4), it is assumed that there is no mass transfer or evaporation across the surface of the fiber, the fluid on the surface remains on the surface at all times. The dynamic conditions include the normal stress condition, Eq. (5),

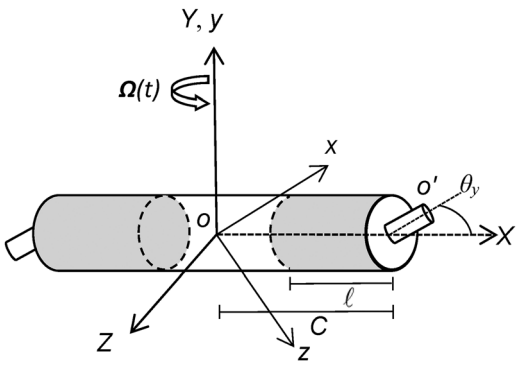

Fig. 2 Spinneret modeled with coordinate systems

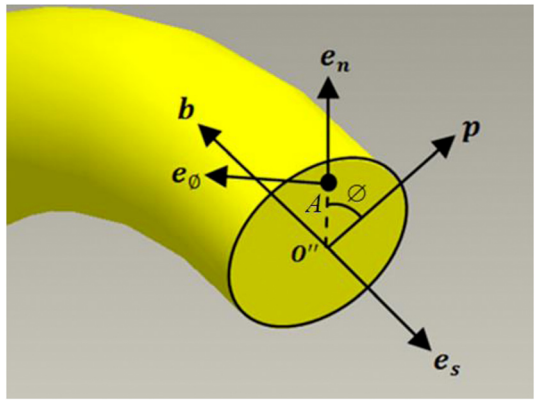

Fig. 3 Depiction of the jet with the curvilinear coordinate system [26]

and the tangential stress conditions, Eqs. (6) and (7). The normal stress condition has the pressure at a free surface balanced by the curvature force associated with the surface tension. The tangential stress conditions are set equal to zero, assuming that there are no forces associated with air drag on the surface.

3 Two-Dimensional Inviscid Forcespinning Model

The fluid dynamics model of the FS system needs first establishing the coordinate systems (Fig. 2). Two coordinate systems were first established, one fixed *xyz*, and the other attached to the rotating spinneret *XYZ*. A two-dimensional model of the FS system is developed. It is assumed that the rotational forces associated with the system are much greater than the gravitational forces on the jet. The viscoelastic properties of the material were also neglected in this work. These assumptions provided the following Euler equations:

$$\frac{\partial \mathbf{u}}{\partial t} + (\mathbf{u}\bullet\nabla)\mathbf{u} = -\frac{\nabla P}{\rho} - \boldsymbol{\omega} \times (\boldsymbol{\omega} \times \mathbf{r}) - 2\boldsymbol{\omega} \times \mathbf{u} \tag{11}$$

The half-length of the spinneret was described by C (center-to-orifice distance, Fig. 2) and the radius of the orifice by r. The axis of rotation is aligned with point O, while point O' represents the point along the X-axis at which the orifice is located. The spinneret is said to rotate about the Y-axis, providing an angular velocity, $\boldsymbol{\omega} = 0\boldsymbol{i} + \Omega\boldsymbol{j} + 0\boldsymbol{k}$. The origin is set to O', defining the position vector of the centerline of the jet as, $\mathbf{r} = (X + C)\boldsymbol{i} + Z\boldsymbol{k}$, where X and Z are the coordinates of a jet centerline current point with respect to the rotating Cartesian coordinate system *XYZ*. Two coordinate systems are used to describe the location of any point A along the jet as proposed by Wallwark et al. [14], Fig. 3. Unit vectors $\boldsymbol{p}$ and $\boldsymbol{e_s}$ are kept on the XZ plane, and the unit vector $\boldsymbol{b}$ in the direction orthogonal to both. The unit vector $\boldsymbol{e_n}$ is in the radial direction of point A, and unit vector $\boldsymbol{e}_{\varnothing}$ is orthogonal to $\boldsymbol{e_n}$ and $\boldsymbol{e_s}$. The radius of the jet is described by R, and point A is described by the radial distance n. The curvilinear unit vectors of the jet are given by

$$\boldsymbol{e_s} = X_s\boldsymbol{i} + Z_s\boldsymbol{k} \tag{12}$$

$$\boldsymbol{e_n} = Z_s \cos\phi\boldsymbol{i} - \sin\phi\boldsymbol{j} - X_s \cos\phi\boldsymbol{k} \tag{13}$$

$$\boldsymbol{e}_{\phi} = -Z_s \sin\phi\boldsymbol{i} - \cos\phi\boldsymbol{j} + X_s \sin\phi\boldsymbol{k} \tag{14}$$

where ϕ is the angle between the unit vector $\boldsymbol{p}$ and unit vector $\boldsymbol{e}_n$. The position vector of any point A within the jet is given by

$$\boldsymbol{r}_A = \int_0^S \boldsymbol{e_s} ds + n\boldsymbol{e_n} \tag{15}$$

where S is the arc length between the spinneret orifice O' and point O'', Figs. 2 and 3.

Next, the equations of the model are nondimensionlized. The dimensionless variables and parameters used afterward have the star superscript and are given as follows:

$$u^* = \frac{u}{U}, \quad v^* = \frac{v}{U}, \quad w^* = \frac{w}{U}, \quad X^* = \frac{X}{C}, \quad Z^* = \frac{Z}{C}, \quad R^* = \frac{R}{r},$$
$$s^* = \frac{s}{C}, \quad n^* = \frac{n}{r}$$
$$\varepsilon = \frac{r}{C}, \quad P^* = \frac{P}{\rho U^2}, \quad \Omega^* = \frac{\Omega C}{U}, \quad t^* = \frac{tU}{C} \tag{16}$$

$$\mathrm{We} = \frac{\rho U^2 r}{\sigma}, \quad \mathrm{Rb} = \frac{U}{\Omega C} \tag{17}$$

where U is the exit speed of the jet in the rotating frame, u tangential velocity (along $\boldsymbol{e_s}$), v radial velocity (along $\boldsymbol{e_n}$), w azimuthal velocity (along $\boldsymbol{e}_{\varnothing}$) of the jet, ρ material density, σ surface tension, P pressure, t time, r radius of the orifice, and ε aspect ratio. In this model, there are two dimensionless numbers, We and Rb, defined in Eq. (17). To derive the equations of motion, one starts with the continuity equation, Eq. (1), where $\mathbf{u}$ is the velocity of the jet given by

$$\mathbf{u} = u\boldsymbol{e_s} + v\boldsymbol{e_n} + w\boldsymbol{e}_{\varnothing} \tag{18}$$

where the operator ∇ in the curvilinear coordinate system is defined as

$$\nabla = \frac{\boldsymbol{e_i}}{h_i}\frac{\partial}{\partial \eta_i} \tag{19}$$

and η_i are the coordinates s, n, and ϕ, and where h_i are scale factors as follows:

$$h_i = \left|\frac{\partial \mathbf{r}_a}{\partial \eta_i}\right| \tag{20}$$

The three scale factors after nondimensionalizing the equations are given by

$$h_n^* = 1, \quad h_{\varnothing}^* = rn^*, \quad h_s^* = 1 + \varepsilon n^* \cos\varnothing(X_s^* Z_{ss}^* - Z_s^* X_{ss}^*) \tag{21}$$

where the subscript s for X and Z denotes the derivative with respect to the arc length. Substituting Eqs. (16), (18), and (19) into equation Eq. (1), the following dimensionless continuity equation results:

$$\varepsilon n^* \frac{\partial u^*}{\partial s^*} + [1 + \varepsilon n^* \cos\varnothing(X_s^* Z_{ss}^* - Z_s^* X_{ss}^*)] \cdot \left(v^* + n^* \frac{\partial v^*}{\partial n^*} + \frac{\partial w^*}{\partial \varnothing}\right)$$
$$+ \varepsilon n^* (X_s^* Z_{ss}^* - Z_s^* X_{ss}^*)(v^* \cos\varnothing - w^* \sin\varnothing) = 0 \tag{22}$$

Solving the Euler equation, Eq. (11), in the same manner, and converting $\boldsymbol{\omega}$ and $\mathbf{r}$ to curvilinear coordinates, the following three dimensionless curvilinear coordinate equations corresponding to $\boldsymbol{e_s}$, $\boldsymbol{e_n}$, and $\boldsymbol{e}_{\varnothing}$ directions result

$$[1 + \varepsilon n^* \cos\varnothing(X_s^* Z_{ss}^* - Z_s^* X_{ss}^*)]\left[\varepsilon \frac{\partial u^*}{\partial t^*} + \varepsilon u^*(X_{st}^* X_s^* + Z_{st}^* Z_s^*) + \varepsilon v^* \cos\varnothing(Z_{st}^* X_s^* - X_{st}^* Z_s^*) + \frac{w^*}{n^*}\frac{\partial u^*}{\partial \varnothing} + v^* \frac{\partial u^*}{\partial n^*}\right.$$
$$\left. + \varepsilon w^* \sin\varnothing(X_{st}^* Z_s^* - Z_{st}^* X_s^*)\right] + \varepsilon u^* v^* \cos\varnothing(X_s^* Z_{ss}^* - Z_s^* X_{ss}^*) - \varepsilon u^* w^* \sin\varnothing(X_s^* Z_{ss}^* - Z_s^* X_{ss}^*)$$
$$+ \varepsilon u^* \frac{\partial u^*}{\partial s^*} = -\varepsilon \frac{\partial P}{\partial s^*} + [1 + \varepsilon n^* \cos\varnothing(X_s^* Z_{ss}^* - Z_s^* X_{ss}^*)]\left[\varepsilon \frac{2}{\mathrm{Rb}}(v^* \cos\varnothing - w^* \sin\varnothing) + \frac{\varepsilon}{\mathrm{Rb}^2}\{(X^* + 1)X_s + Z^* Z_s\}\right] \tag{23}$$

$$[1+\varepsilon n^*\cos\varnothing(X_s^*Z_{ss}^*-Z_s^*X_{ss}^*)]\left[\varepsilon\frac{\partial v^*}{\partial t^*}+\varepsilon u^*\cos\varnothing(X_{st}^*Z_s^*-Z_{st}^*X_s^*)+\varepsilon v^*\cos^2\varnothing(X_{st}^*X_s^*+Z_{st}^*Z_s^*)+\frac{w^*}{n^*}\frac{\partial v^*}{\partial\varnothing}\right.$$
$$\left.-\varepsilon w^*\cos\varnothing\sin\varnothing(X_{st}^*X_s^*-Z_{st}^*Z_s^*)-\frac{w^{*2}}{n^*}-\frac{w^*}{n^*}\sin\varnothing(X_t^*Z_s^*-X_s^*Z_t^*)+v^*\frac{\partial v^*}{\partial n^*}\right]$$
$$+\varepsilon u^*\frac{\partial v^*}{\partial s^*}+\varepsilon u^*v^*\cos\varnothing(X_s^*Z_{ss}^*-Z_s^*X_{ss}^*)-\varepsilon u^*w^*\sin\varnothing(X_s^*Z_{ss}^*-Z_s^*X_{ss}^*)$$
$$-\varepsilon u^{*2}\cos\varnothing(X_s^*Z_{ss}^*-Z_s^*X_{ss}^*)=[1+\varepsilon n^*\cos\varnothing(X_s^*Z_{ss}^*-Z_s^*X_{ss}^*)]\left[-\frac{\partial P}{\partial n^*}-\varepsilon\frac{2}{\mathrm{Rb}}u^*\cos\varnothing+\varepsilon\frac{\cos\varnothing}{\mathrm{Rb}^2}\{(X^*+1)Z_s-Z^*X_s+\varepsilon n^*\cos\varnothing\}\right] \tag{24}$$

$$[1+\varepsilon n^*\cos\varnothing(X_s^*Z_{ss}^*-Z_s^*X_{ss}^*)]\left[\varepsilon\frac{\partial w^*}{\partial t^*}+\varepsilon u^*\sin\varnothing(Z_{st}^*X_s^*-X_{st}^*Z_s^*)-\varepsilon v^*\cos\varnothing\sin\varnothing(X_{st}^*X_s^*+Z_{st}^*Z_s^*)\right.$$
$$\left.+v^*\frac{\partial w^*}{\partial n^*}+\varepsilon w^*\sin^2\varnothing(X_{st}^*X_s^*+Z_{st}^*Z_s^*)+\frac{v^*w^*}{n^*}+\frac{v^*}{n^*}\sin\varnothing(X_t^*Z_s^*-X_s^*Z_t^*)+\frac{w^*}{n^*}\frac{\partial w^*}{\partial\varnothing^*}\right]+\varepsilon u^*\frac{\partial w^*}{\partial s^*}$$
$$+\varepsilon u^{*2}\sin\varnothing(X_s^*Z_{ss}^*-Z_s^*X_{ss}^*)=[1+\varepsilon n^*\cos\varnothing(X_s^*Z_{ss}^*-Z_s^*X_{ss}^*)]\left[-\frac{1}{n^*}\frac{\partial P}{\partial\varnothing}+\varepsilon\frac{2}{\mathrm{Rb}}u^*\sin\varnothing\right.$$
$$\left.+\varepsilon\frac{\sin\varnothing}{\mathrm{Rb}^2}\{-(X^*+1)Z_s+Z^*X_s-\varepsilon n^*\cos\varnothing\}\right] \tag{25}$$

Using Eqs. (4)–(7), the kinematic and dynamic jet boundary conditions are to be solved. The kinematic condition, Eq. (4), is solved by substituting for the definition of β, which describes the free surface of the jet. The assumption is made that there is no material loss at the surface (no evaporation). For the dynamic conditions, since the jet is said to be inviscid, the tangential stresses at a free surface are not present, and only the normal stress equation, Eq. (5), is used. Equations (6) and (7) will be considered in future work. For the inviscid case, the normal stress dynamic condition, Eq. (5), simplifies to

$$P=\sigma\cdot k \quad \text{on} \quad n=R(s,\varnothing,t) \tag{26}$$

This equation is then solved using Eqs. (8) and (9) for k. The dimensionless kinematic and dynamic conditions on the jet surface are given by Eqs. (27) and (28), respectively,

$$v^*=\varepsilon\frac{\partial}{\partial t^*}(R^*-n^*)+\varepsilon\frac{\mu^*}{h_s^*}\frac{\partial R^*}{\partial s^*}+\frac{w^*}{n^*}\frac{\partial R^*}{\partial\varnothing} \tag{27}$$

$$P^*=\frac{1}{We\cdot h_s{}^*n^*}\left[\varepsilon^2\frac{\partial}{\partial s^*}\left(\frac{-\frac{n^*}{h_s^*}\frac{\partial R^*}{\partial s^*}}{|\nabla\beta^*|}\right)+\frac{\partial}{\partial n^*}\left(\frac{h_s^*n^*}{|\nabla\beta^*|}\right)\right.$$
$$\left.+\frac{\partial}{\partial\varnothing}\left(\frac{-\frac{h_s^*}{n^*}\frac{\partial R^*}{\partial\varnothing}}{|\nabla\beta^*|}\right)\right] \tag{28}$$

where

$$\left|\nabla\beta^*\right|=\sqrt{\frac{\varepsilon^2}{h_s{}^{*2}}\left[\frac{\partial R^*}{\partial s^*}\right]^2+\frac{1}{n^{*2}}\left[\frac{\partial R^*}{\partial\varnothing}\right]^2+1} \tag{29}$$

Equations (22)–(25), (27), (28), and Eq. (3) with $Y_s=0$ form a system of seven differential equations with four independent variables s^*, n^*, $\varnothing$, t^* and seven dependent variables u^*, v^*, w^*, P^*, R^*, X^*, Z^*.

4 Method of Multiple Scales

The method of multiple scales is used to approximate the solutions of the derived equations using ε as the small parameter. The expansions are done assuming slender jet theory. These equations also assume that the angular velocity of the spinneret is constant. Also, the azimuthal motion of the jet is assumed to be zero (the fiber does not twist) [14]. "Twisting is immaterial in centrifugal spinning," [39]. First, the steady-state equations are derived and solved. The steady-state equations are used to determine the effect of We and Rb numbers on the jet trajectory, jet radius R, and the tangential component u of the jet velocity. The steady-state equations are also used to determine the effect of the jet exit angle on the jet formation. Second, the leading-order approximation with time-dependent parameters are solved and compared with the steady-state solutions. The effects of changing the controllable parameters in FS using dimensional values are then determined. The approximation of the time-dependent equations is done using a fast and slow time scale, T_o and T_1, respectively. The variables are expanded as follows:

$$u^*=u_o^*(s^*,T_o,T_1)+\varepsilon u_1^*(s^*,n^*,\varnothing,T_o,T_1)+\cdots \tag{30}$$

$$v^*=\varepsilon v_o^*(s^*,n^*,\varnothing,T_o,T_1)+\varepsilon^2 v_1^*(s^*,n^*,\varnothing,T_o,T_1)+\cdots \tag{31}$$

$$P^*=P_o^*(s^*,n^*,\varnothing,T_o,T_1)+\varepsilon P_1^*(s^*,n^*,\varnothing,T_o,T_1)+\cdots \tag{32}$$

$$R^*=R_o^*(s^*,T_o,T_1)+\varepsilon R_1^*(s^*,\varnothing,T_o,T_1)+\cdots \tag{33}$$

$$X^*=X_o^*(s^*,T_o,T_1)+\varepsilon X_1^*(s^*,T_o,T_1)+\cdots \tag{34}$$

$$Z^*=Z_o^*(s^*,T_o,T_1)+\varepsilon Z_1^*(s^*,T_o,T_1)+\cdots \tag{35}$$

where v_o^* is assumed to be in the ε approximation due to the slender jet theory [42].

5 Constant Rotation Steady-State Solutions

Solving for the steady-state equations by using the method of multiple scales, the following system of ordinary differential equations that depend only on the arc length s along the jet results

$$u_o^*u_{os}^*=-\frac{\partial}{\partial s^*}\left(\frac{1}{R_o{}^*We}\right)+\frac{1}{Rb^2}[(X_o^*+1)X_{os}^*+Z_o^*Z_{os}] \tag{36}$$

$$u_o^{*2}\left(X_{os}^*Z_{oss}^*-Z_{os}^*X_{oss}^*\right)=\frac{1}{R_o{}^*We}\left(X_{os}^*Z_{oss}^*-Z_{os}^*X_{oss}^*\right)+\frac{2}{Rb}u_o^*$$
$$+\frac{1}{Rb^2}[Z_o^*X_{os}^*-(X_o^*+1)Z_{os}^*] \tag{37}$$

$$X_{os}^{*}X_{oss}^{*} = -Z_{os}^{*}Z_{oss}^{*} \tag{38}$$

$$u_{o}^{*}R_{os}^{*} = -\frac{R_{o}^{*}}{2}u_{os}^{*} \tag{39}$$

The equations are solved using ode45, an ordinary differential equations solver in MATLAB. Initial conditions ($s=0$) are based on the assumption that the jet leaves the orifice along the X-direction with speed U. Also, the radius of the jet is assumed to be the same as the radius of the orifice r at the exit point, O'. The dimensionless initial conditions are as follows:

$$X_{o}^{*} = Z_{o}^{*} = Z_{os}^{*} = 0, \quad X_{os}^{*} = R_{o}^{*} = u_{o}^{*} = 1 \quad \text{at} \quad s = 0 \tag{40}$$

The effect of the jet exit angle θ_y (Fig. 2) on the jet formation is modeled by changing the unit tangent vector of the jet when exiting the spinneret ($s=0$) as follows:

$$Z_{os}^{*} = -\sin\theta_y \;\; X_{os}^{*} = \cos\theta_y \quad \text{at} \quad s = 0 \tag{41}$$

for Eqs. (36)–(39) of steady-state motion. The focus is to determine whether there is an optimal angle at which the final jet diameter can be minimized. The reference direction for the jet exit angle is along the longitudinal axis of the spinneret. The jet exit angle is positive in the direction of rotation (Fig. 2). For instance, if the jet exits along the spinneret axis, the angle is said to be 0 deg. If the jet exit is perpendicular to the spinneret axis and oriented in the same direction with the rotation, its angle is said to be 90 deg. If perpendicular to the spinneret axis and oriented in the opposite direction of the rotation, the angle is said to be −90 deg.

6 Constant Rotation Time-Dependent Solutions

In this section, Eqs. (23)–(25) are solved by including the time-dependent components, therefore removing the assumption that the first approximation does not depend on time. The method of multiple scales is used in the case of constant angular velocity. Similar equations to those for steady-state Eqs. (36)–(39) are obtained as follows:

$$u_{ot}^{*} + u_{o}^{*}u_{os}^{*} = -\frac{\partial}{\partial s^{*}}\left(\frac{1}{R_{o}^{*}\mathrm{We}}\right) + \frac{1}{\mathrm{Rb}^{2}}\left\{\left(X_{os}^{*}+1\right)X_{os}^{*} + Z_{o}^{*}Z_{os}^{*}\right\} \tag{42}$$

$$R_{ot}^{*} + u_{o}^{*}R_{os}^{*} = -\frac{R_{o}^{*}}{2}u_{os}^{*} \tag{43}$$

$$u_{o}^{*2}\left(X_{os}^{*}Z_{oss}^{*} - Z_{os}^{*}X_{oss}^{*}\right) = \frac{1}{R_{o}^{*}We}\left(X_{os}^{*}Z_{oss}^{*} - Z_{os}^{*}X_{oss}^{*}\right) + \frac{2}{Rb}u_{o}^{*} + \frac{1}{Rb^{2}}\left(Z_{o}^{*}X_{os}^{*} - \left(X_{o}^{*}+1\right)Z_{os}^{*}\right) \tag{44}$$

$$X_{os}^{*}X_{oss}^{*} = -Z_{os}^{*}Z_{oss}^{*} \tag{45}$$

where u_{ot}^{*} and R_{ot}^{*} are time derivatives of the relative velocity and jet radius, respectively. The system of partial differential equations (Eqs. (42)–(45)) is then solved using the method of lines

Table 1 Physical parameters used for the system

Parameter	Symbol	Value
Half-length of spinneret	C	0.0657 m
Orifice radius	r	0.0000795 m
Jet density	ρ	1000 kg/m^3
Surface tension	σ	0.072 N/m
Angular velocity	Ω	314 rad/s

Table 2 Dimensionless parameters used for the system

Parameter	Symbol	Value
Rossby number	Rb	1
Weber number	We	469.93

[43]. The time derivatives of the tangential component of the jet velocity and the jet radius are approximated using the finite difference method as follows:

$$u_{ot}{}^{*} = \frac{u_{i+1}^{*} - u_{i}^{*}}{\Delta t^{*}} \tag{46}$$

$$R_{ot}^{*} = \frac{R_{i+1}^{*} - R_{i}^{*}}{\Delta t^{*}} \tag{47}$$

This produces a group of ordinary differential equations that depend only on the arc length s.

7 Numerical Simulations

Material properties used in the numerical simulations with those of water, since it can be approximated as inviscid, are shown in Table 1, which gives dimensional properties used in these simulations. Table 2 shows the calculated We and Rb numbers.

7.1 Steady-State Solutions, We, Rb and Exit Angle Effects.

Using Eqs. (36)–(40), the effects of We and Rb on the jet trajectory, jet radius, and tangential component of jet velocity are investigated and results are shown in Figs. 4 and 5, Figs. 6 and 7, and Figs. 8 and 9, respectively. The values for We and Rb numbers were chosen in such a way that they will describe realistic FS conditions of the inviscid case. The Rb values of 1.0, 0.866, and 0.66 result from Eq. (17) and afterward Eq. (47) for three cases, namely, full spinneret, half-full spinneret, and quarter-full spinneret, respectively. The possible Rb values for FS are between 0 and 1, since Rb values greater than 1 can only exist from internal expelling pressures within the spinneret, which are not present in this system. The values for We result from three angular velocities, namely, 32.5, 45.8, 144.9 rad/s, for water and the orifice of the spinneret of 79.5 μm.

Figures 4 and 5 show the effects of Rb and We on the jet trajectory. As Rb increases and/or We increases, the jet trajectory expands outward. This is in agreement with Wallwork et al. [14] who reported that "smaller Rossby numbers and smaller Weber

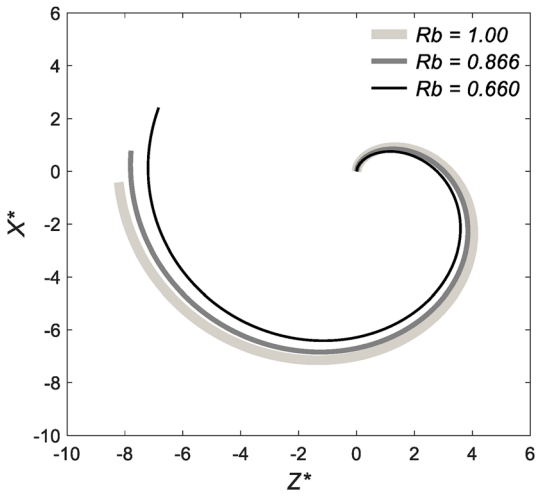

Fig. 4 Effect of the Rossby number on the jet trajectory, We = 100

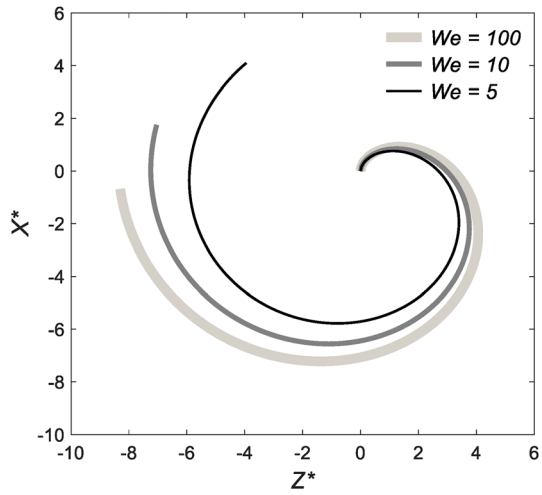

Fig. 5 Effect of the Weber number on the jet trajectory, Rb = 1

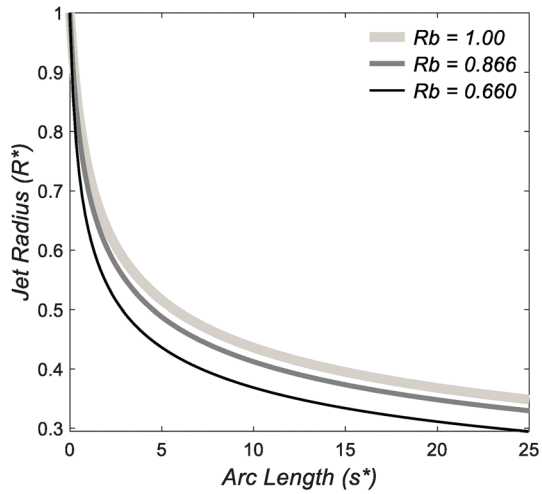

Fig. 6 Effect of the Rossby number on the jet radius along the arc length, We = 100

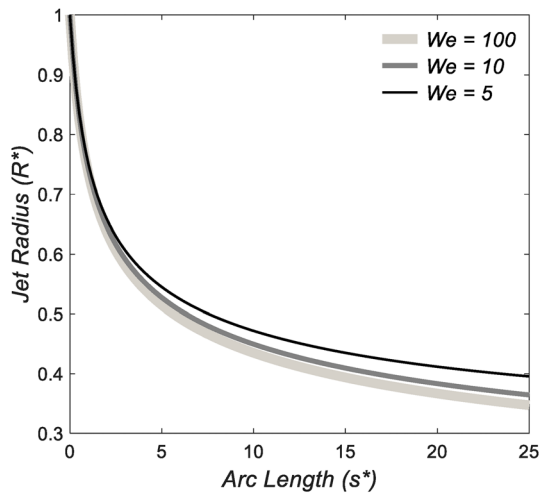

Fig. 7 Effect of the Weber number on the jet radius along the arc length, Rb = 1

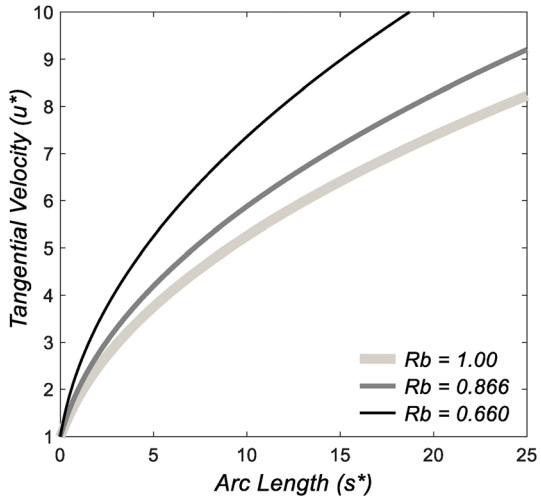

Fig. 8 Effect of the Rossby number on the tangential velocity along the arc length, We = 100

numbers correspond to more tightly coiled loops," and Noroozi et al. [39] who reported that "We significantly influences the jet behaviors: the fiber trajectory is much tighter compared to higher We, up to a point that the fiber even reaches a circular trajectory centered on the axis of rotation." Figures 6 and 7 show the effects of Rb and We on the jet radius. As Rb decreases and/or We increases, the jet radius decreases. This is in agreement with Wallwork et al. [14] and Noroozi et al. [39] who reported that "the fiber starts to thin much more quickly for smaller Rb, and the fiber thinning rate at shorter arc lengths is weaker for smaller We."

Figures 8 and 9 show an opposite effect of Rb and We on the jet tangential velocity. The tangential velocity increases with the decrease of Rb and/or the increase of We. Rb is the ratio between the exit velocity U of the jet and the angular velocity Ω of the spinneret, and We is directly proportional to the square of the velocity and the orifice radius, Eq. (17).

Figures 4, 6, and 8 show that for the same angular velocity Ω, as Rb decreases from 1 to 0.66 due to the fluid level inside the spinneret reduction from full to half, then to a quarter (1), the jet tangential velocity increases as the radius of the jet decreases, which is consistent with the continuity equation, and (2) the jet trajectory contracts, which is consistent with the increase in the Coriolis effect. Figures 5, 7, and 9 show that for the same orifice radius as the angular velocity Ω decreases (U decreases, so We

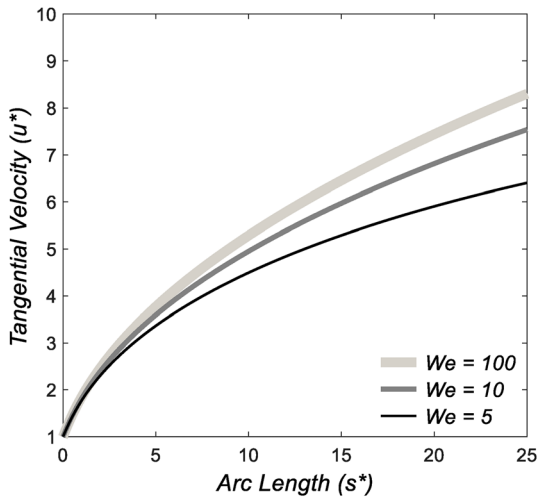

Fig. 9 Effect of the Weber number on the tangential velocity along the arc length, Rb = 1

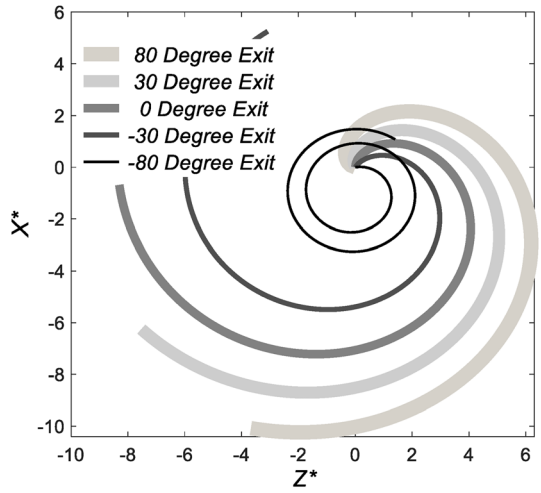

Fig. 10 Jet trajectories using We = 100 and Rb = 1 at varying jet exit angles

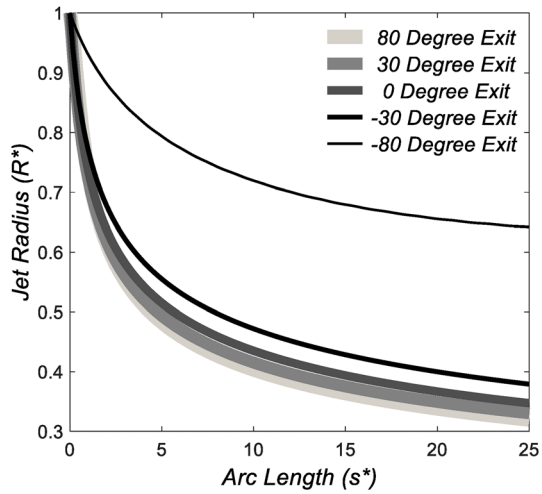

Fig. 11 Radius versus arc length using We = 100 and Rb = 1 at varying jet exit angles

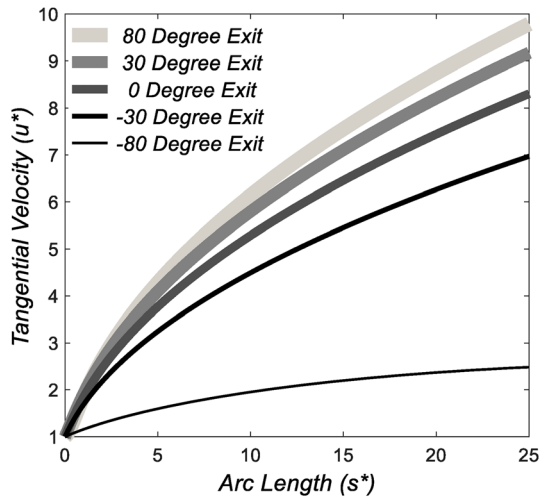

Fig. 12 Tangential velocity versus arc length using We = 100 and Rb = 1 at varying jet exit angles

decreases) (1), the jet tangential velocity decreases and the radius of the jet increases, which is consistent with the continuity equation, and (2) the jet trajectory contracts, which is consistent with the decrease in the centrifugal effect. Close to the orifice, the rate of change of the tangential component of velocity, with respect to the arc length s is higher for small Rb (Fig. 8), which results in a higher reduction rate of the jet radius (Fig. 6).

Next, the effect of the jet exit angle θ_y on the jet formation is investigated (Figs. 10–12). Numerical simulations were conducted for exit angles between −80 deg and 80 deg. Figure 10 shows the effect of the jet exit angle on the jet trajectory. This is in good agreement with experimental data reported in the literature: "as the angle increases in the direction of the rotation, the trajectory of the jet expands outward," [31]. Figure 11 shows the effect of the exit angle on the jet radius. As the exit angle increases from −80 deg to 80 deg, the jet radius decreases. The radius decrease becomes less significant between the exit angles in the range of 0 deg and 80 deg. Figure 12 shows that the tangential velocity increases with the increase in the exit angle. These results clearly show a relationship between the jet exit angle and the resulting jets. As the orifice is angled in the direction of rotation, the Coriolis force acting on the jet as it leaves the orifice has a positive component along the outward direction of the spinneret, see positive x-axis in Fig. 2. Therefore, the jet experiences larger outward

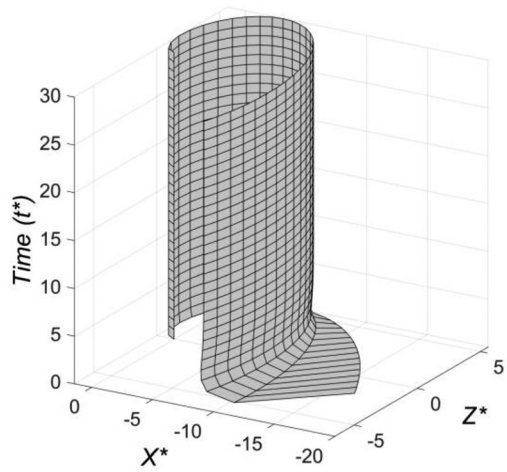

(*a*)

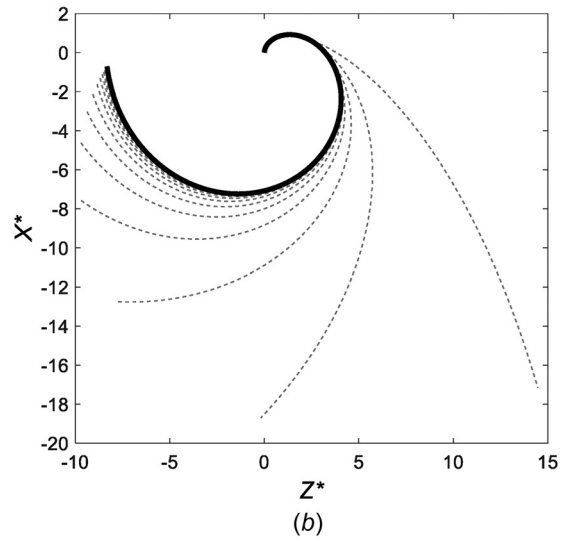

(*b*)

Fig. 13 Results over 30 time units at 1.0 time intervals with We = 100 and Rb = 1: (*a*) jet trajectory over time and (*b*) jet trajectory approximation to steady-state (top view)

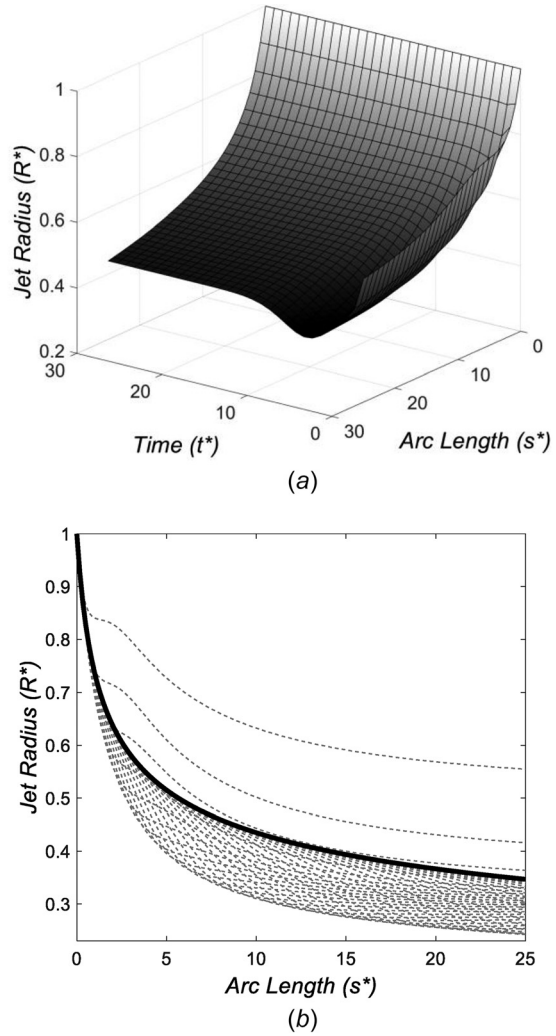

Fig. 14 Results over 30 time units at 1.0 time intervals with We = 100 and Rb = 1: (*a*) jet radius over arc length and time and (*b*) jet radius versus arc length approximation to steady-state

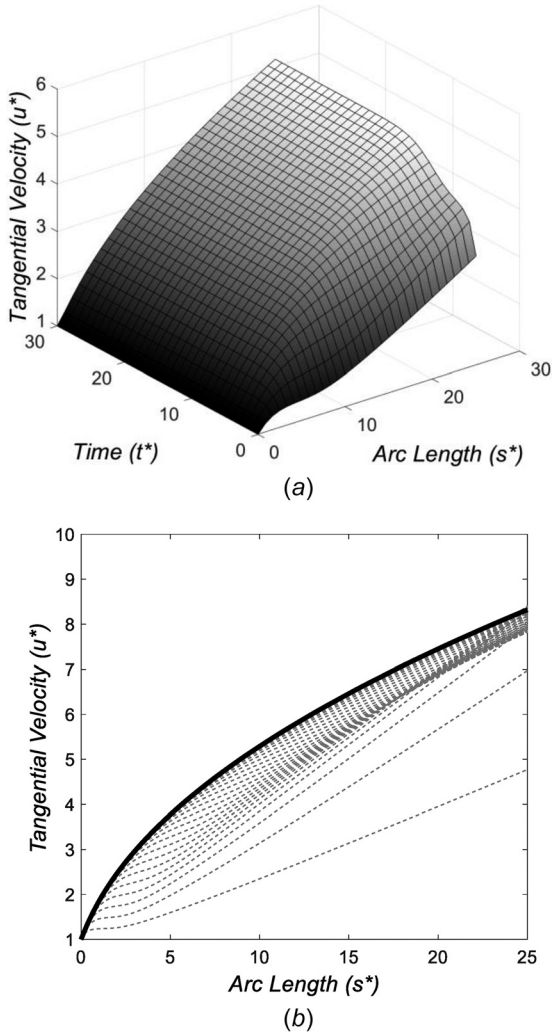

Fig. 15 Results over 30 time units at 1.0 time intervals with We = 100 and Rb = 1: (*a*) jet tangential velocity over arc length and time and (*b*) jet trajectory versus arc length approximation to steady-state

forces and faster tangential component of velocity, which results in thinner jets. Conversely, if the orifice is angled in the opposite direction of rotation, the Coriolis force acting on the jet as it leaves the spinneret has a component on the inward direction of the spinneret, see negative x-axis in Fig. 2. This reduces the centrifugal forces on the jet and results in a contraction of trajectory as showed in Fig. 10. Although the nanofiber production during FS requires viscoelastic effects to be included, the trend of these results will help in optimizing the system and obtaining fiber diameters that are as small as possible.

7.2 Time-Dependent Solutions. Numerical simulations for time dependent solutions, Eqs. (42)–(47), were conducted using a MATLAB ODE solver, namely, *ode45*. The jet is set initially straight with a constant radius (the radius of the orifice) throughout its length. The system is solved with We = 100 and Rb = 1 and iterated over a span of 30 dimensionless time units, a dimensionless arc length of 25, and a time-step of 1.0. The resulting trajectory, jet radius, and velocity as they evolve over time and arc length are shown in Fig. 13–15, respectively. The results for the time-dependent equations show the trajectory, radius, and velocity approaching the steady-state solutions over time, as expected, Figs. 13(*b*) and 4, 14(*b*) and 6, and 15(*b*) and 8, respectively. The time-dependent equations verify the initial assumption that the jet formation can be determined assuming that the governing

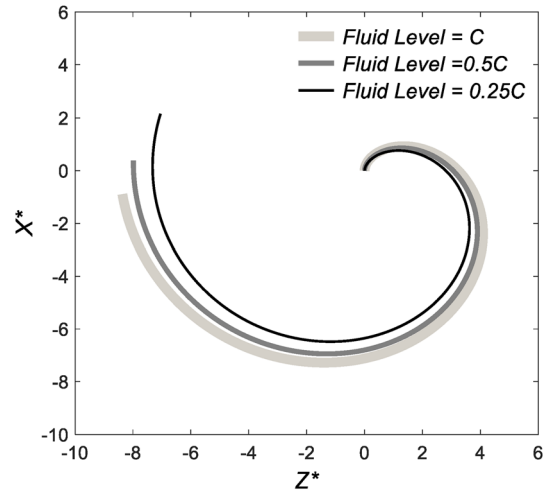

Fig. 16 Effect of the fluid level on the trajectory, using $C = 0.0657$ m, $r = 79.5\,\mu$m, $\rho = 1000$ kg/m^3, $\sigma = 0.072$ N/m, and $\Omega = 314$ rad/s

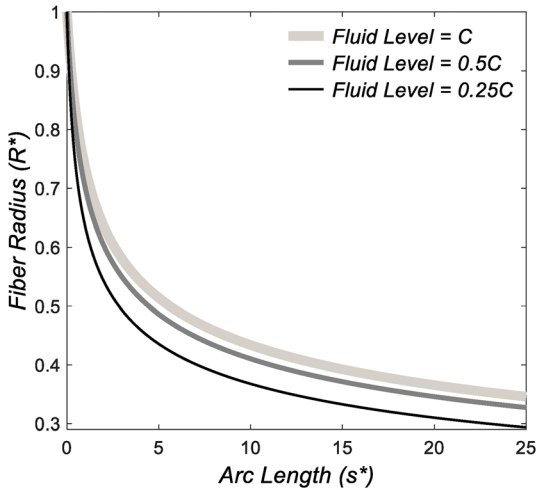

Fig. 17 Effect of the fluid level on the jet radius using $C = 0.0657$ m, $r = 79.5\,\mu$m, $\rho = 1000$ kg/m^3, $\sigma = 0.072$ N/m, and $\Omega = 314$ rad/s

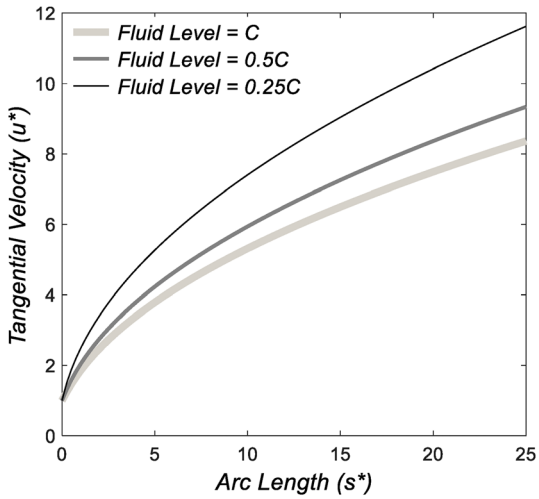

Fig. 18 Effect of the fluid level on the jet tangential velocity using $C = 0.0657$ m, $r = 79.5\,\mu$m, $\rho = 1000$ kg/m^3, $\sigma = 0.072$ N/m, and $\Omega = 314$ rad/s

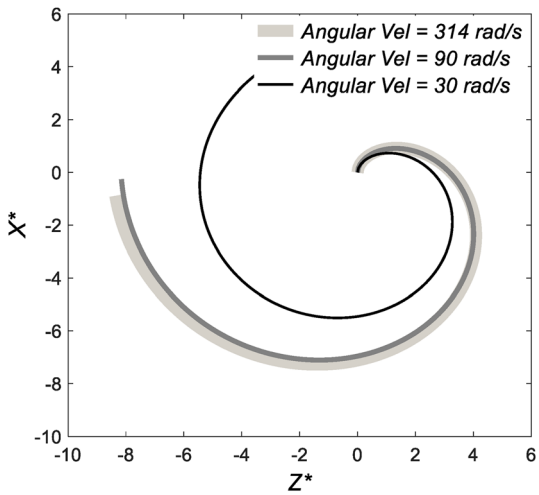

Fig. 19 Effect of the spinneret angular velocity (Ω) on the jet trajectory using $C = 0.0657$ m, $r = 79.5\,\mu$m, $\rho = 1000$ kg/m^3, and $\sigma = 0.072$ N/m

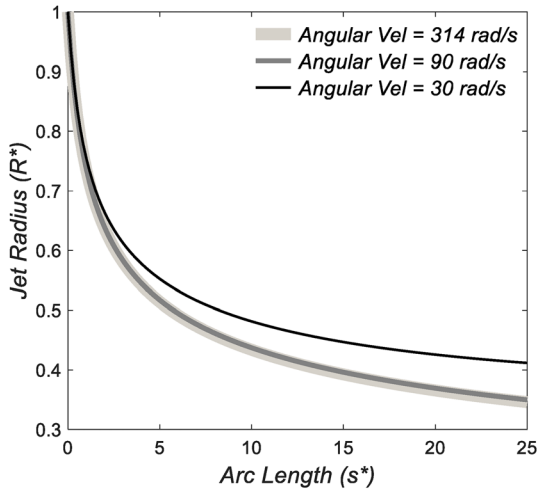

Fig. 20 Effect of the spinneret angular velocity (Ω) on the jet radius using $C = 0.0657$ m, $r = 79.5\,\mu$m, $\rho = 1000$ kg/m^3, and $\sigma = 0.072$ N/m

equations do not depend on time once a constant angular velocity is reached. These time-dependent equations can later be used for investigating forcespinning with nonconstant angular velocities.

7.3 Effects of Fluid Level, Angular Velocity, Orifice Radius, and Half-Length. This section uses dimensional values associated with FS to provide a better understanding of the effects that various controllable parameters have on the jet trajectory, radius, and tangential component of the velocity.

First, the time-independent model (Eqs. (36)–(39)) is used to determine the effect of the amount of fluid in the spinneret (fluid level) on jet formation. The corresponding dimensionless We and Rb numbers for these values are shown in Table 2. For the same angular velocity of the spinneret, the exit velocity of the jet changes with the amount of fluid present within the container as it is being forcespun. The relationship between fluid level ℓ given in Fig. 2 and exit velocity U for an inviscid fluid is as follows:

$$U = \Omega\sqrt{2C\ell - \ell^2} \tag{48}$$

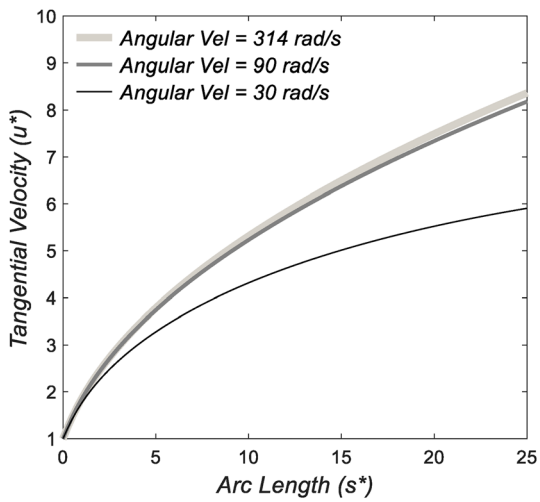

Fig. 21 Effect of the spinneret angular velocity (Ω) on the jet tangential velocity using $C = 0.0657$ m, $r = 79.5\,\mu$m, $\rho = 1000$ kg/m^3, and $\sigma = 0.072$ N/m

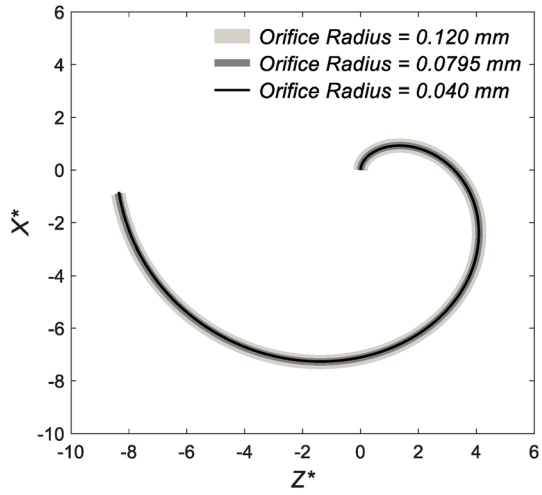

Fig. 22 Effect of the orifice radius (*r*) on the jet trajectory using $U = 20.63$ m/s, $C = 0.0657$ m, $\rho = 1000$ kg/m^3, $\sigma = 0.072$ N/m, and $\Omega = 314$ rad/s

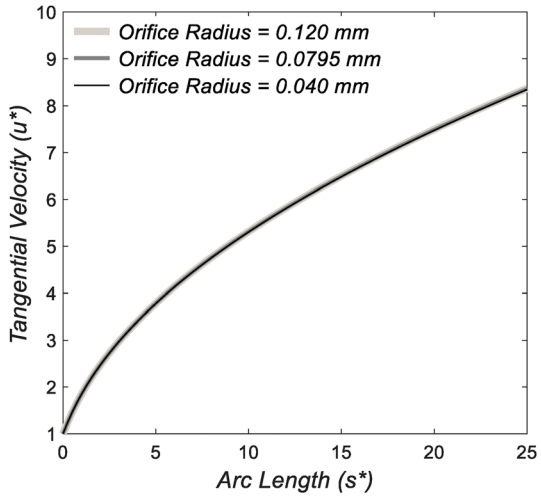

Fig. 24 Effect of the orifice radius (*r*) on the jet tangential velocity using $C = 0.0657$ m, $\rho = 1000$ kg/m^3, $\sigma = 0.072$ N/m, and $\Omega = 314$ rad/s

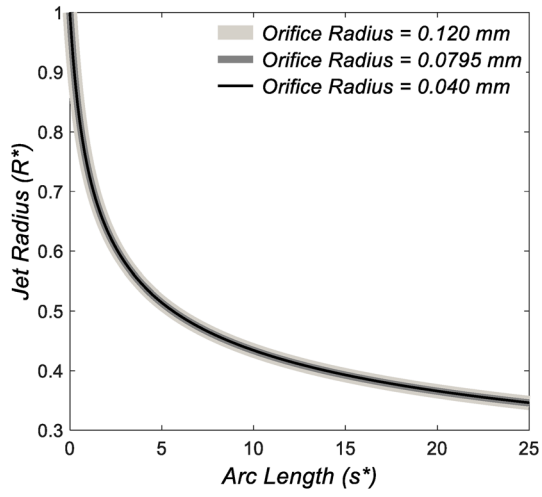

(*a*)

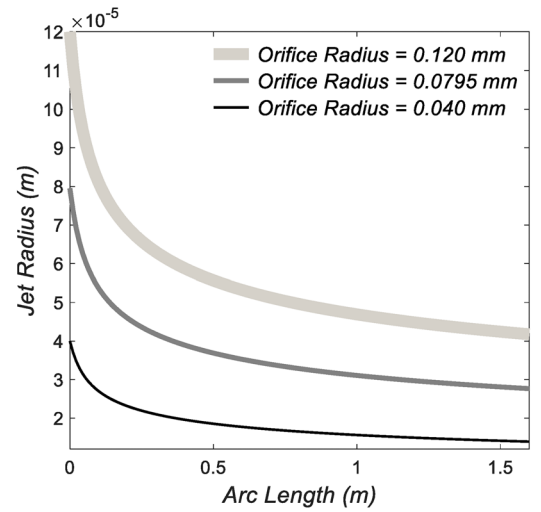

(*b*)

Fig. 23 Effect of the orifice radius (*r*) on the jet radius using C = .0657 m, $\rho = 1000$ kg/m^3, $\sigma = .072$ N/m, and $\Omega = 314$ rad/s: (*a*) dimensionless and (*b*) dimensional

where $0 \leq \ell \leq C$. Numerical simulations were conducted for three different values of fluid level ℓ, namely, $0.25C$, $0.50C$, and C, corresponding to exit velocities of 13.65 m/s, 17.87 m/s, and 20.63 m/s, respectively. The exit velocity equation is derived by setting forces in equilibrium and using the Darcy–Weisbach equation [44] with the special case of no viscosity. When the container is full, $\ell = C$, the exit velocity is $U = \Omega C$. The effects of the fluid level on the jet trajectory, radius, and tangential velocity is shown in Figs. 16–18, respectively. Figure 16 is in good agreement with experimental data reported in the literature: "as the fluid fill level increases, the fiber expels further outward" [31]. Conversely, by reducing the amount of fluid in the spinneret, the jet trajectory contracts and gets closer to the spinneret. An interesting result can be seen in Fig. 17. The radius of the produced jet is seen to decrease as the fluid fill is reduced. This shows that in continuous feeding systems, lowering the feeding rate will have the effect of producing thinner jets.

Second, the effect of the angular velocity of the spinneret on the jet formation is investigated (see Figs. 19–21). These figures show that as the angular velocity of the spinneret is increased, the trajectory expands, the jet radius decreases, and the tangential velocity increases. The outward expanding trajectory and the decrease in the jet radius are in good agreement with experimental data reported in the literature studies [31,45].

Third, the effect of the orifice radius on jet formation has been investigated. The values for orifice radius r considered in the numerical simulations were 40 μm, 79.5 μm, and 120 μm. The orifice radius has no significant effect on the dimensionless trajectories (Fig. 22), the dimensionless jet radius (Fig. 23(*a*)), or the dimensionless tangential velocities (Fig. 24), since the angular velocity and fluid level were kept the same. Using $R^* = {}^{R}/_{r}$, for 42 μm, for the 40 μm, 79.5 μm, and 120 μm orifice radii, the dimensional radii of the jet at the dimensionless arc length of 25 are 14 μm, 28 μm, and 42 μm, respectively (Fig. 23(*b*)). It makes sense that using smaller orifices will produce smaller jet diameters, as the stretching starts with a thinner original radius. However, for viscous fluids, there is a lower threshold below which clogging may occur. Therefore, the forces needed to produce a jet are much larger. This can be compensated with higher angular velocities.

Fourth, the effect of the half-length, C, of the spinneret on the jet formation is investigated. Three different half-length dimensions are used, namely, 0.03 m, 0.0657 m, and 0.09 m. One can see that the length of the spinneret does not have a significant effect on the dimensionless trajectory (Fig. 25(*a*)) and

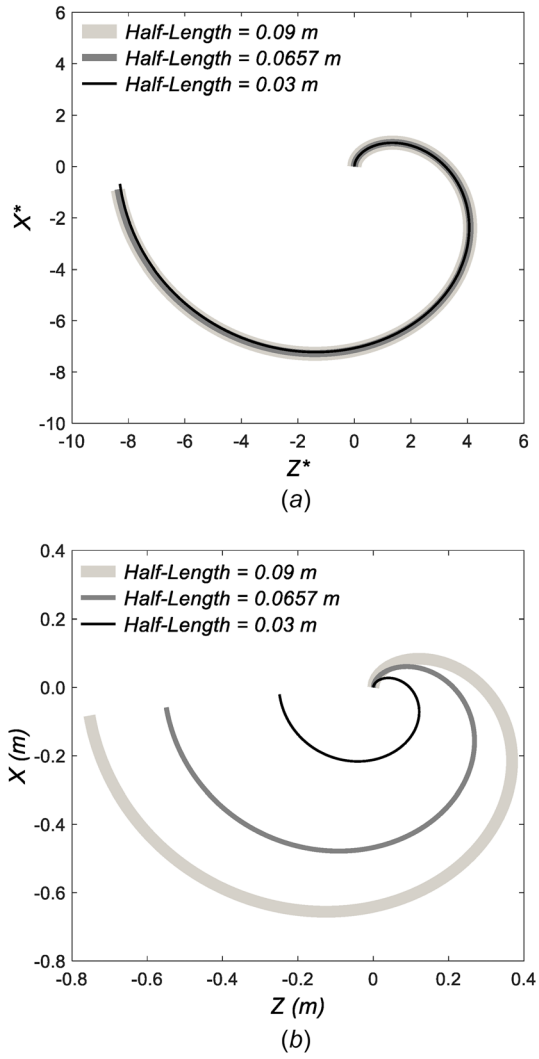

Fig. 25 Effect of the spinneret radius or half length (*C*) on the jet trajectory using $r = 79.5\,\mu$m, $\rho = 1000$ kg/m^3, $\sigma = 0.072$ N/m, and $\Omega = 314$ rad/s: (*a*) dimensionless and (*b*) dimensional

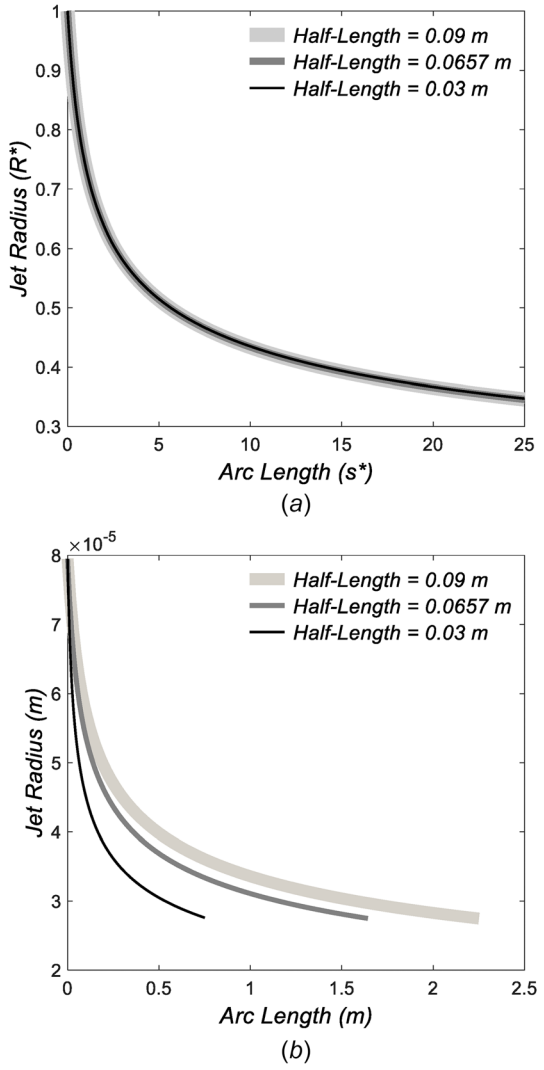

Fig. 26 Effect of the spinneret radius or half-length (*C*) on the jet radius using $r = 79.5\,\mu$m, $\rho = 1000$ kg/m^3, $\sigma = 0.072$ N/m, and $\Omega = 314$ rad/s: (*a*) dimensionless and (*b*) dimensional

dimensionless jet radius (Fig. 26(*b*)). Using the dimensional relationships, $x^* = {}^{x}/_{C}$ and $z^* = {}^{z}/_{C}$, it is seen that by increasing the length of the spinneret, the dimensional trajectories expand further outward (Fig. 25(*b*)). This can be explained by the larger centrifugal forces experienced as you increase the distance from the center of rotation. Regarding Figs. 26(*b*) and 27(*b*), since the dimensionless arc length s^* is considered to be the same and the length of the spinneret ($2C$) changes, the dimensional arc length $s = s^*C$ changes as well. For example, at $s^* = 25$, the dimensionless jet radius is 35% of the original for all three (see Fig. 26(*a*)). Then, converting these arc lengths to dimensional values s gives jet lengths of 0.75 m, 1.64 m, and 2.25 m. Figure 26(*b*) shows that as the length of the spinneret decreases, the radius of the resulting jet becomes smaller and decreases at a faster rate, while Fig. 27(*b*) shows that the tangential velocity decreases with a decrease in the spinneret length.

7.4 Effects of Arc Length and Numerical Tolerance. Figures 28–30 show the effect of arc length s on the trajectory, radius, and tangential velocity. They also show that for large tolerances in the simulations, numerical instabilities occur. As the tolerance is considered as small as 10^{-9}, the simulations show a consistent jet behavior in all three figures. Moreover, Fig. 31 shows the volume flow rate of the jet, which should be constant due to continuity equation. For small tolerance 10^{-9} in the numerical simulations, the volume flow rate is constant, while for larger tolerance 10^{-3}, the volume flow rate does not remain constant. Therefore, a tolerance of 10^{-3} gives erroneous results for large arc lengths. The consistent results in Figs. 28–30 are for a tolerance of 10^{-9}.

Two outcomes of interest for FS are the jet radius R and the corresponding distance D from the center of rotation, point O in Fig. 2. The distance D can be determined as follows:

$$D = \sqrt{(X + C)^2 + Z^2} \tag{49}$$

where X and Z are the coordinates or the jet position at which the radius is R. The radius of the collector of the jets plays an important role in the jet production, Fig. 32. For instance, if the collector is designed to start collecting at an arc length $s^* = 25$, then its radius is $D^* = 7.5$, the radius of the jet is $R^* = 0.35$, and the tangential velocity is $u^* = 8.5$. These are dimensionless values. The corresponding dimensional values are $s = 1.64$ m, $D = 0.49$ m, $R = 27.8\,\mu$m, and $u = 175$ m/s. For this case, the production rate is given by the tangential velocity. Therefore, a production rate of u

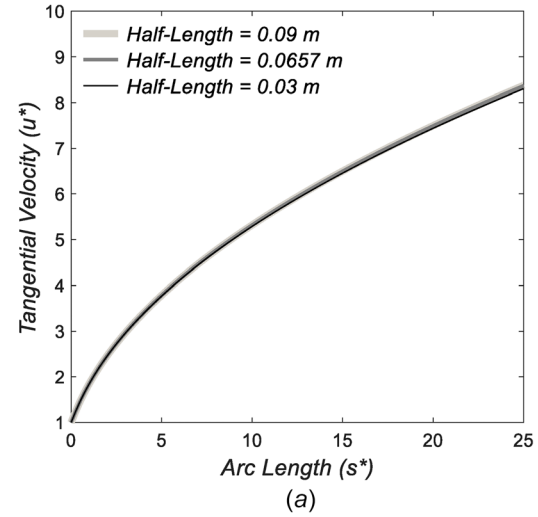

(*a*)

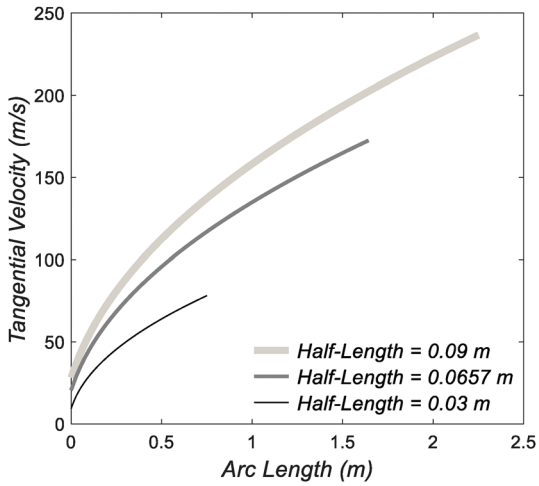

(*b*)

Fig. 27 Effect of the spinneret radius or half-length (*C*) on the jet tangential velocity using $r = 79.5\,\mu$m, $\rho = 1000\,$kg/m^3, $\sigma = 0.072\,$N/m, and $\Omega = 314\,$rad/s: (*a*) dimensionless and (*b*) dimensional

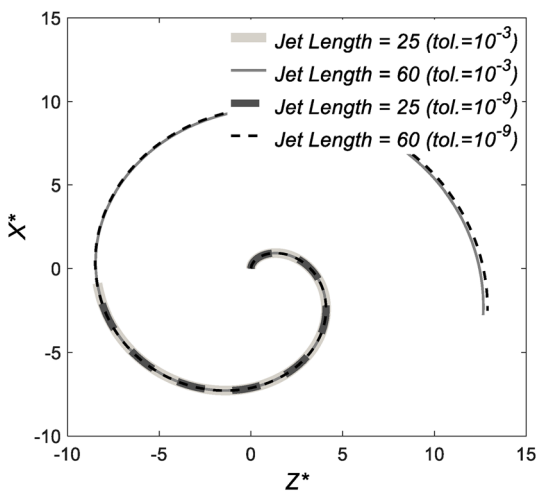

Fig. 28 Trajectory comparison computed at different jet lengths and tolerances

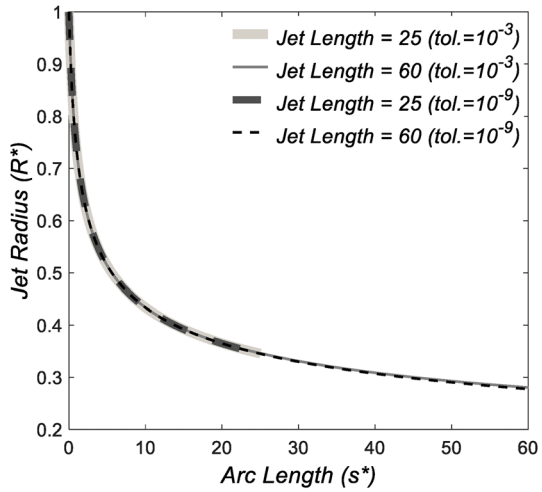

Fig. 29 Radius comparison computed at different jet lengths and tolerances

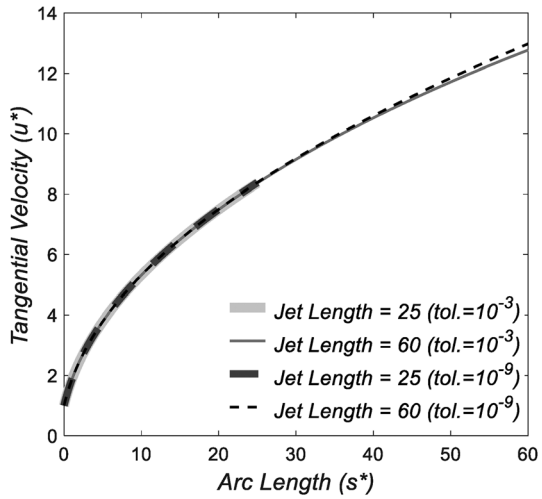

Fig. 30 Tangential velocity comparison computed at different jet lengths and tolerances

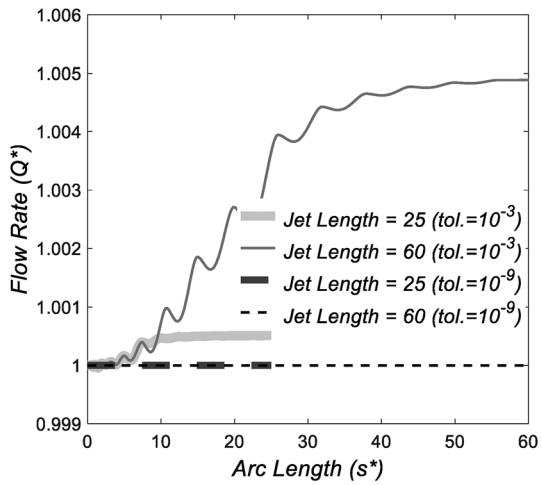

Fig. 31 Flow rate comparison computed at different jet lengths and tolerances

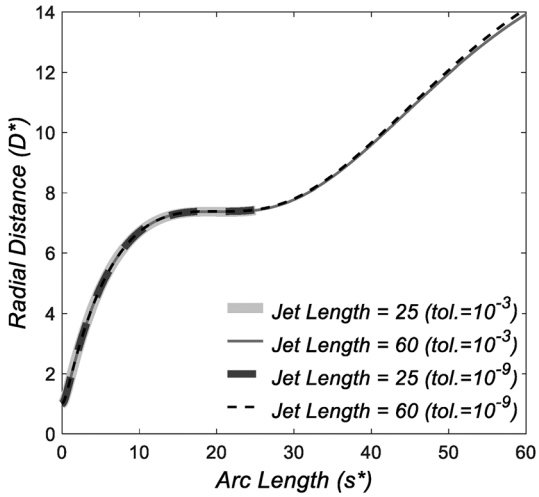

Fig. 32 Radial distance comparison computed at different jet lengths and tolerances

$=175$ m/s for a jet of radius $R=27.8\ \mu$m is obtained at a collector radial distance of 0.49 m.

8 Discussion and Conclusions

The governing equations for the nanofiber production method of FS were derived for a 2D inviscid model. The inviscid steady-state solutions and their stability were in good agreement with data reported in the literature studies [14,26,31]. The steady-state equations were used to determine the effect of Rb and We numbers on the jet trajectory and jet radius. It has been found that the jet trajectories expand outward with the increase in Rb and/or We, while the jet radius increases with the increase in Rb and/or the decrease in We. This is in agreement with data reported in the literature, Wallwark et al. [14] and Decent et al. [15]. The novelty of this work consists of the FS model to include a radial collector, the variation of the jet exit angle, the inclusion of fluid level within the container, the inclusion of the tangential velocity of the jet to the differential equations, providing a method for determining production rates, and the solution to the partial differential equations including the time-derivatives of tangential velocity and radius, providing solutions over the arc length and time. It has been shown that the trajectory of the jet expands outward with (1) the increase in the jet exit angle in the direction of rotation, (2) the increase in the fluid level, and (3) the increase in the angular velocity. This is in agreement with experimental data reported in the literature [31]. It was found that smaller jet diameters may be obtained by increasing the jet exit angle in the direction of rotation. For the time-dependent solutions, the numerical simulations describe the expected results of approaching the steady-state solutions. The time-dependent model can also be used to investigate the case of nonconstant angular velocities. The dimensional values gave trends that matched that of experimental results [31]. The dimensional values provided an insight into the FS process, which can be used to improve the uniformity of the jets and to reduce the final diameter sizes as much as possible. Also, the jet production rate and radius for any predetermined collector distance were solved. This information will be important for further optimization of the FS system. The ability to accurately predict the final diameter of nanofibers using the FS method is in progress, with these initial models laying the foundation on which to continue introducing parameters that will more accurately predict physical results.

A few of the limitations of this forcespinning model are (1) it is an inviscid model, (2) it does not account for jet diameter reduction at the orifice (in the experimental work by Padron et al. [38], it is observed that the initial jet radius in FS becomes considerably lower than that of the orifice), (3) does not include gravity, (4) does not account for solvent evaporation, and (5) jet break-up is not accounted for (since for future improvements to the FS model, viscous effects will be included along with the assumption that fibers will be continuously collected). Increasing the orifice radius has minor effects in this model, as no losses are present since viscosity is neglected.

Future work will include viscosity into the model, evaporation effects, and forces associated with air drag on the surface. The time-dependent model will be used to examine the effect of non-constant angular velocity on forcespinning jet formation.

Funding Data

- National Science Foundation (DMR Grant # 0934157; Funder ID: 10.13039/100000001).

References

[1] Duan, Y.-Y., Jia, J., Wang, S.-H., Yan, W., Jin, L., and Wang, Z.-Y., 2007, "Preparation of PLGA Electrospun Nanofibers for Tissue Engineering Applications," J. US-China Med. Sci., **4**(1), pp. 41–44.

[2] Kim, K., Yu, M., Zong, X., Chiu, J., Fang, D., Seo, Y.-S., Hsiao, B. S., Chu, B., and Hadjiargyrou, M., 2003, "Control of Degradation Rate and Hydrophilicity in Electrospun Non-Woven Poly(D, L-Lactide) Nanofiber Scaffolds for Biomedical Applications," Biomaterials, **24**(27), pp. 4977–4985.

[3] Kowalewski, T. A., Barral, S., and Kowalczy, T., 2009, "Modeling Electrospinning of Nanofibers," IUTAM Symp. Modell. Nanomaterials Nanosystems (IUTAM Bookseries), **13**, pp. 279–292.

[4] Lyons, J. M., 2004, "Melt Electrospinning of Thermoplastic polymers - An Experimental and Theoretical Analysis," Ph.D. thesis, Drexel University, Philadelphia, PA.

[5] Thompson, C. J., Chase, G. G., Yarin, A. L., and Reneker, D. H., 2007, "Effects of Parameters on Nanofiber Diameter Determined From Electrospinning Model," Polymer, **48**(23), pp. 6913–6922.

[6] Xu, L., 2009, "A Mathematical Model for Electrospinning Process Under Coupled Field Forces," Chaos, Solitons Fractals, **42**(3), pp. 1463–1465.

[7] Yarin, A. L., Koombhongse, S., and Reneker, D. H., 2001, "Taylor Cone and Jetting From Liquid Droplets in Electrospinning of Nanofibers," J. Appl. Phys., **90**(9), pp. 4836–4846.

[8] Nagai, Y., Unsworth, L., Koutsopoulos, S., and Zhang, S., 2006, "Slow Release of Molecules in Self-Assembling Peptide Nanofiber Scaffold," J. Controlled Release, **115**(1), pp. 18–25.

[9] Rayleigh, J. W. S., 1878, "On the Instability of Jets," Proc. London Math. Soc., **s1–10**(1), pp. 4–13.

[10] Weber, C., 1931, "To the Disintegration of a Liquid Jet (Zum Zerfall Eines Flüssigkeitsstrahles)," Z. Angew. Math. Mech., **11**(2), pp. 136–141.

[11] Eggers, J., 1997, "Nonlinear Dynamics and Breakup of Free-Surface Flows," Rev. Mod. Phys., **69**(3), pp. 865–929.

[12] Ozgen, S., and Uzol, O., 2012, "Investigation of the Linear Stability Problem of Electrified Jets, Inviscid Analysis," ASME J. Fluids Eng., **134**(9), p. 0912019.

[13] Grafe, T., and Graham, K., 2003, "Polymeric Nanofibers and Nanofiber Webs: A New Class of Nonwovens," Int. Nonwovens J., **12**(1), pp. 51–55.

[14] Wallwork, I. M., Decent, S. P., King, A. C., and Schulkes, R. M. S. M., 2002, "The Trajectory and Stability of a Spiraling Liquid Jet: Part I—Inviscid Theory," J. Fluid Mech., **459**, pp. 43–65.

[15] Decent, S. P., King, A. C., and Wallwork, I. M., 2002, "Free Jets Spun From a Prilling Tower," J. Eng. Math, **42**(3/4), pp. 265–282.

[16] Uddin, J., and Decent, S. P., 2009, "Curved Non-Newtonian Liquid Jets With Surfactants," ASME J. Fluids Eng., **131**(9), p. 091203.

[17] Dravid, V., Loke, P. B., Corvalan, C. M., and Sojka, P. E., 2008, "Drop Formation in Non-Newtonian Jets at Low Reynolds Numbers," ASME J. Fluids Eng., **130**(8), p. 081504.

[18] Ahmed, M., Abou-Al-Sood, M. M., and Ali, A. H. H., 2011, "A One-Dimensional Model of Viscous Liquid Jets Breakup," ASME J. Fluids Eng., **133**(1), p. 114501.

[19] Barhoum, A., Pal, K., Rahier, H., Uludag, H., Kim, I. S., and Bechelany, M., 2019, "Nanofibers as New-Generation Materials: From Spinning and Nano-Spinning Fabrication Techniques to Emerging Applications," Appl. Mater. Today, **17**, pp. 1–35.

[20] Carroll, C. P., and Joo, Y. L., 2006, "Electrospinning of Viscoelastic Boger Fluids: Modeling and Experiments," Phys. Fluids, **18**(5), p. 053102.

[21] Feng, J. J., 2002, "The Stretching of an Electrified Non-Newtonian Jet: A Model for Electrospinning," Phys. Fluids, **14**(11), pp. 3912–3926.

[22] Feng, J. J., 2003, "Stretching of a Straight Electrically Charged Viscoelastic Jet," J. Non-Newtonian Fluid Mech., **116**(1), pp. 55–70.

[23] Reneker, D. H., Yarin, A. L., Fong, H., and Koombhongse, S., 2000, "Bending Instability of Electrically Charged Liquid Jets of Polymer Solution in Electrospinning," J. Appl. Phys., **87**(9), pp. 4531–4547.

[24] Theron, S. A., Yarin, A. L., Zussman, E., and Kroll, E., 2005, "Multiple Jets in Electrospinning: Experiment and Modeling," Polymer, **46**(9), pp. 2889–2899.

[25] Părău, E. I., Decent, S. P., Simmons, M. J. H., Wong, D. C. Y., and King, A. C., 2007, "Nonlinear Viscous Liquid Jets From a Rotating Orifice," J. Eng. Math., **57**(2), pp. 159–179.
[26] Padron, S., Caruntu, D. I., and Lozano, K., 2011, "On 2-D Forcespinning Modeling," ASME Paper No. IMECE2011-64823.
[27] Panda, S., Marheineke, N., and Wegener, R., 2008, "Systematic Derivation of an Asymptotic Model for the Dynamics of Curved Viscous Fibers," Math. Methods Appl. Sci., **31**(10), pp. 1153–1173.
[28] Padron, S., and Caruntu, D. I., 2012, "Influence of Viscosity on Forcespinning Dynamics," Proceedings of International Mechanical Engineering Congress and Exposition, Nov. 9–15, Houston, TX, Paper No. IMECE2012-85964.
[29] Taghavi, S. M., and Larson, R. G., 2014, "Regularized Thin-Fiber Model for Nanofiber Formation by Centrifugal Spinning," Phys. Rev. E, **89**(2), p. 023011.
[30] Riahi, D., 2017, "Modeling and Computation of Nonlinear Rotating Polymeric Jets During Forcespinning Process," Int. J. Non-Linear Mech., **92**, pp. 1–7.
[31] Padron, S., Fuentes, A. A., Caruntu, D. I., and Lozano, K., 2013, "Experimental Study of Nanofiber Production Through Forcespinning," J. Appl. Phys., **113**(2), p. 024318.
[32] Ziabicki, K., 1976, *Fundamentals of Fiber Formation*, Wiley, New York.
[33] Denn, M. M., 1980, "Continuous Drawing of Liquids to Form Fibers," Annu. Rev. Fluid Mech., **12**(1), pp. 365–387.
[34] Denn, M. M., 2009, "Simulation of Polymer Melt Processing," AIChE J., **55**(7), pp. 1641–1647.
[35] Hyun, J. C., 1978, "Theory of Draw Resonance—Part I: Newtonian Fluids," AIChE J., **24**(3), pp. 418–422.
[36] Pearson, J. R. A., 1976, "Instability in Non-Newtonian Flow," Annu. Rev. Fluid Mech., **8**(1), pp. 163–181.
[37] Petrie, C. J. S., and Denn, M. M., 1976, "Instabilities in Polymer Processing," AIChE J., **22**(2), pp. 209–239.
[38] Zhou, C., and Kumar, S., 2010, "Thermal Instabilities in Melt Spinning of Viscoelastic Fibers," J. Non-Newtonian Fluid Mech., **165**(15–16), pp. 879–891.
[39] Noroozi, S., Alamdari, H., Arne, W., Larson, R. G., and Taghavi, S. M., 2017, "Regularized String Model for Nanofibre Formation in Centrifugal Spinning Methods," J. Fluid Mech., **822**, pp. 202–234.
[40] Osswald, T., and Hernández-Ortíz, J. P., 2006, *Polymer Processing-Modeling and Simulation*, Hanser Publishers, Munich, Germany.
[41] Furlani, E. P., Delametter, C. N., Chwalek, J. M., and Trauernicht, D. P., 2001, "Surface Tension Induced Instability of Viscous Liquid Jets," Proceeding of the Fourth International Conference on Modeling and Simulation of Microsystems, Hilton Head Island, SC, Mar. 19–21, pp. 186–189.
[42] Ting, L., and Keller, J. B., 1990, "Slender Jets and Thin Sheets With Surface Tension," SIAM J. Appl. Math., **50**(6), pp. 1533–1546.
[43] Schiesser, W. E., and Griffiths, G. W., 2009, *A Compendium of Partial Differential Equation Models: Method of Lines Analysis With Matlab*, Cambridge University Press, New York.
[44] Balachandran, P., 2011, *Engineering Fluid Mechanics*, Prentice Hall of India, New Delhi, India.
[45] Padron, S., Patlan, R., Gutierrez, J., Santos, N., Eubanks, T., and Lozano, K., 2012, "Production and Characterization of Hybrid BEH-PPV/PEO Conjugated Polymer Nanofibers by Forcespinning," J. Appl. Polym. Sci., **125**(5), pp. 3610–3616.